rotational patterns under axial loading were consolidated into 10 directions, which provides insight into the subject-specific kinematics of the tibiotalar joint.

Keywords: Tibiotalar joint; Three-dimensional bone model; Weight bearing; Kinematics.

INTRODUCTION

Three-dimensional (3D) alignment of the talus relative to the tibia at the tibiotalar joint under axial-loaded conditions is different from that under unloaded conditions.[6,7,10] Under axial loading, the talus receives the axial load and transmits it to the calcaneus and navicular.[8,9] In this process, the talus rotates three-dimensionally relative to the tibia at the tibiotalar joint. To investigate the load response of the joint, many studies[6,7,10] have quantified talus rotations relative to the tibia at this joint under axial loading. These studies[6,7,10] show that whether the talus rotates into inversion or eversion and into adduction or abduction relative to the tibia at the tibiotalar joint under axial loading remains controversial.

Essentially, the talus may have some rotational directions relative to the tibia under axial loading. Several probable factors determine the rotational directions of the tibiotalar joint, including the morphological variations in the talus[8,9,12] and calcaneus.[1–5,11,13–15] However, assuming that the tibiotalar joint has only one rotational direction in intact feet, the previous results[6,7,10] describing its rotations under axial loading along three axes were combined as an average even if the talus is rotated into plantarflexion or dorsiflexion in the sagittal plane, into inversion or eversion in the coronal plane, and into adduction or abduction in the transverse plane. All eight rotational patterns of the tibiotalar joint during axial loading were consolidated into systematic directions. Identifying the 3D distribution of the rotational directions of the tibiotalar joint would help to identify the factors that determine subject-specific kinematics of the tibiotalar joint. In addition, identifying the rotational patterns of the tibiotalar joint under axial loading would provide basic information for investigating the subject-specific pathokinematics of the tibiotalar joint in subjects with chronic ankle instability due to ankle sprain and with degenerative changes of the ankle joint. Consequent informed physical therapy may be able to modify such kinematic patterns. However, research regarding 3D movements at the tibiotalar joint is still insufficient. The purpose of the present study was to investigate the three-axis rotational directions of the talus relative to the tibia at the tibiotalar joint in intact feet during axial loading by using 3D reconstructive magnetic resonance imaging (MRI). We hypothesized that 3D rotational motion is different in different individuals and that motion patterns can be categorized according to three-axis rotational directions.

METHODS

Participant Recruitment

A total of 27 intact feet (21 right feet, 6 left feet) in either leg of 27 subjects with a mean age of 23.1 years (range, 20–34 years) were recruited in this study. The exclusion criteria included history of ankle sprain or surgery to the lower extremity, ankle instability, and cartilaginous lesions confirmed by MRI on the tested foot. Ankle instability was judged using the anterior drawer test and/or talar tilt test. Ankles of the dominant leg used to kick a ball were tested. If the exclusion criteria eliminated the dominant ankle, the nondominant ankle was used. All subjects were

explained the purpose of this study, and they signed a consent form approved by the Medical Research Ethics Committee of Sapporo Medical University before participating in the study.

Image Acquisition and 3D Modeling

A loading device (Dynawell L-Spine; Dynawell Diagnostics, Las Vegas, US) was used to apply an axial load of 60% body weight (Fig. 1). The device consisted of three main components: a foot plate, a shoulder vest, and two straps. The axial load was applied to the trunk and lower extremity by changing the distance between the foot plate and shoulder vest. In our preliminary study, we measured the plantar pressure of seven healthy subjects in the standing position and in the loading device by using a pressure distribution measurement platform. Comparison of the center of pressure revealed no significant difference between these two conditions.

The subjects lay on the MRI table keeping their feet, knees, and hips in a neutral position. Both legs and trunk were positioned parallel to the straps, and the centers of the knee and ankle joints were aligned with the load line. MR images were obtained by using a GE Signa HDx 1.5T (GE Healthcare, Milwaukee, WI, USA). Scanning was performed from 10-cm proximal to the inferior edge of the medial malleolus to the talus by using fast imaging with steady-state acquisition (flip angle, 30°; echo time, 3.1 ms; repetition time, 7 ms; matrix, 160 × 160; scan time, 2 min 50 s) with a 15 cm × 15 cm field of view. The slice thickness of the images was 1.0 mm. Under the unloaded condition, the subjects received an axial loading of 2 kg to each foot using the loading device to keep the ankle joint in neutral position, whereas in the loaded condition, the subjects received an axial load of 30% of their body weight to each foot. The mean axial load value applied to each foot was 19.7 ± 2.2 (range, 16–24) kg. All sagittal MR images of the tibia and talus in the Digital Imaging and Communications in Medicine format were exported to a 3D reconstruction software package (Mimics; Materialise Co., Ltd., Yokohama, Japan). Using this software, we segmented the distal tibia and talus on the basis of the threshold level in all sagittal MR images and then created 3D models (Fig. 2).

Setting the Coordinate Systems

Coordinate systems corresponding to the anatomical axes of the tibia and talus were set to describe the orientation of the talus relative to the tibia at the tibiotalar joint by using interactive musculoskeletal modeling software (SIMM; NAC Image Technology Inc., Ltd., Tokyo, Japan). First, an x–y–z coordinate system was set to the tibia according to the anatomical landmarks of the tibia by using methods described in a previous

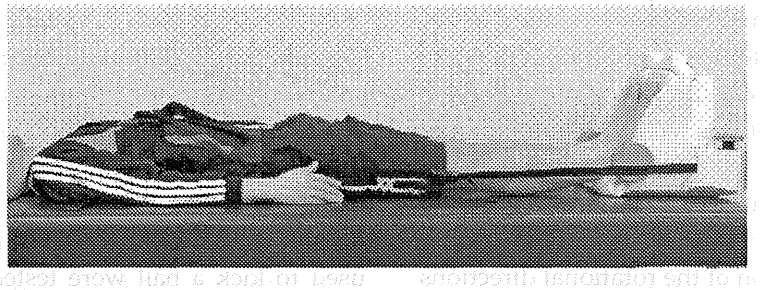

Fig. 1 The loading device used to apply the axial load to the body. Axial loads that were equivalent to 60% body weight were applied to the subjects by using a loading device that consisted of 3 main components: a foot plate, a shoulder vest, and 2 straps.

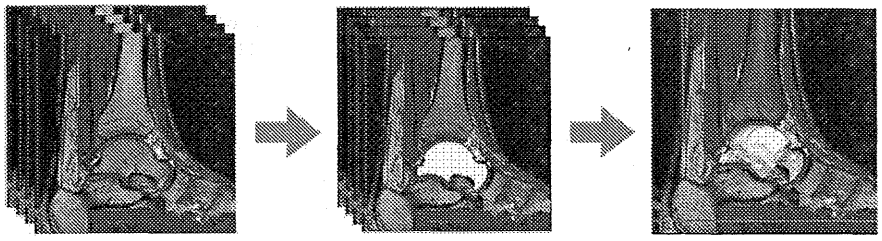

Fig. 2 3D reconstruction of the tibiotalar joint from MRI data. MR images were used to create 3D models of the distal tibia and the talus at the tibiotalar joint. The distal tibia and talus were segmented on the basis of the threshold level in all sagittal MR images.

study[16] (Fig. 3). Second, a coordinate system that had the same orientation as the x-y-z axes was defined for the talus. The x-axis was defined as the plantar/dorsiflexion axis, the y-axis as the inversion/eversion axis, and the z-axis as the adduction/abduction axis.

Kinematic Analysis and Data Processing

After setting the coordinate systems, 3D bone models of the tibiotalar joint under the unloaded and axial-loaded conditions were observed together, and the tibia under the axial-loaded condition was superimposed on that under the unloaded condition [Fig. 4(a)]. Then, the talus under the unloaded condition was superimposed on that in the axial-loaded condition [Fig. 4(b)] to calculate the difference in the rotational orientation of the talus relative to the tibia under the unloaded and axial-loaded conditions. Three-axis rotations of the tibiotalar joint during axial loading were represented as Eulerian angles (Fig. 3) as averages and coefficients of variation were calculated. For analysis of the individual variations

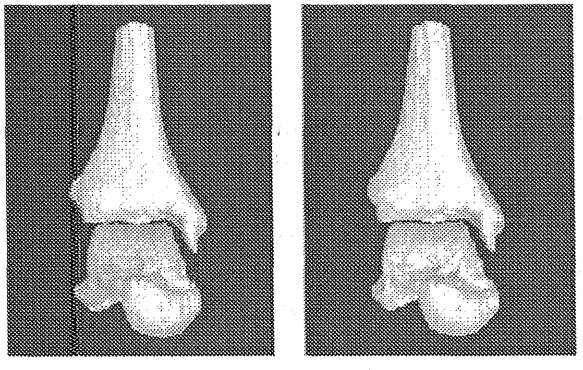

(a) (b)

Fig. 3 x-y-z coordinate system used to define the three-axis rotations at the tibiotalar joint. Plantarflexion, inversion, and adduction are represented by a plus sign, and dorsiflexion, eversion, abduction are represented by a minus sign.

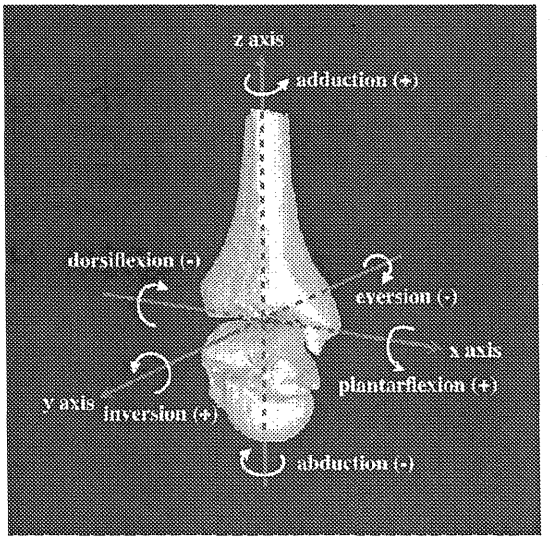

Fig. 4 Superimposition of the 3D models of the tibiotalar joint. **(a)** Anterior view of the right tibiotalar joint. The beige model of the tibiotalar joint represents an unloaded condition. The cyan model of the tibiotalar joint represents an axial-loaded condition. The model of the tibia under the axial-loaded condition was superimposed on that under the unloaded condition **(a)**. Then, the model of the talus under the unloaded condition was superimposed on that under the axial-loaded condition **(b)**.

in rotational directions of the tibiotalar joint, the distributions of the rotational directions of the tibiotalar joint in the three axes were described. In addition, the 3D rotational patterns at the tibiotalar joint were categorized according to the combinations of the rotational directions. In this analysis, 0.5° was the minimum calculated value of relative rotation between the tibia and the talus.

To determine intrarater reliability, one examiner conducted five repeated independent measurements, and the mean error was calculated. The mean errors for the five repeated measurements were 0.05°, 0.02°, and 0.04° in the sagittal, coronal, and transverse planes, respectively.

Statistical Analysis

SPSS software (version 19.0.0, SPSS Inc., Tokyo, Japan) was used to perform the statistical analysis. The chi-squared test was used to investigate the differences in the frequency of the rotation patterns of the tibiotalar joint under the axial-loaded condition. The level of significance was set at $p < 0.05$. Data were expressed as the mean ± standard deviation in the texts, figures, and tables unless noted otherwise.

RESULTS

Differences in the 3D orientation of the talus relative to the tibia at the tibiotalar joint between the unloaded and axial-loaded conditions are summarized in Table 1. The distribution of the number of feet grouped according to the rotational directions of the tibiotalar joint along the three axes under axial-loaded conditions is shown in Figs. 5(a)–5(c). In the sagittal and coronal planes, the talus individually rotated into plantarflexion or dorsiflexion and into inversion or eversion is relative to the tibia, respectively. In contrast, almost all of the talus rotated into adduction relative to the tibia in the transverse plane.

Table 1 Differences in the Orientation of the Talus Relative to the Tibia at the Tibiotalar Joint in the Unloaded and Axial-Loaded Conditions.

Rotational Plane	Average ± SD [Degrees]	Range [Degrees]	Coefficient of Variation
Sagittal (pf/df)	0.9 ± 2.1	−1.8 to 9.0	2.3
Coronal (iv/ev)	0.2 ± 0.9	−1.2 to 3.4	4.5
Transverse (add/abd)	0.9 ± 0.9	−2.6 to 3.0	1

Note: pf: plantarflexion, df: dorsiflexion, iv: inversion, ev: eversion, add: adduction, abd: abduction.

The rotational patterns that were categorized in terms of combinations of the three-axis rotational directions of the tibiotalar joint are shown in Fig. 6. A total of 10 rotational patterns at the tibiotalar joint were observed. Averages of the three-axis rotations at the tibiotalar joint in all 10 rotational patterns are shown in Table 2. Five main rotational patterns were recognized, which accounted for 78% of the feet (pf/iv/add, pf/un/add, pf/ev/add, df/iv/add, df/ev/add, Table 2). The chi-squared test showed no significant differences in the frequency of each of the 10 rotational patterns of the tibiotalar joint ($p > 0.05$).

DISCUSSION

This is the first study to investigate the distribution of the three-axis rotational directions of the tibiotalar joint under axial loading in intact feet. We observed variations in coronal and sagittal rotational directions of the tibiotalar joint under axial loading, whereas almost all of the talus consistently rotated into adduction in the transverse plane relative to the tibia at the tibiotalar joint.

There were a few limitations in this study. First, the axial load applied was 60% of body weight. So the acquired values of the talus

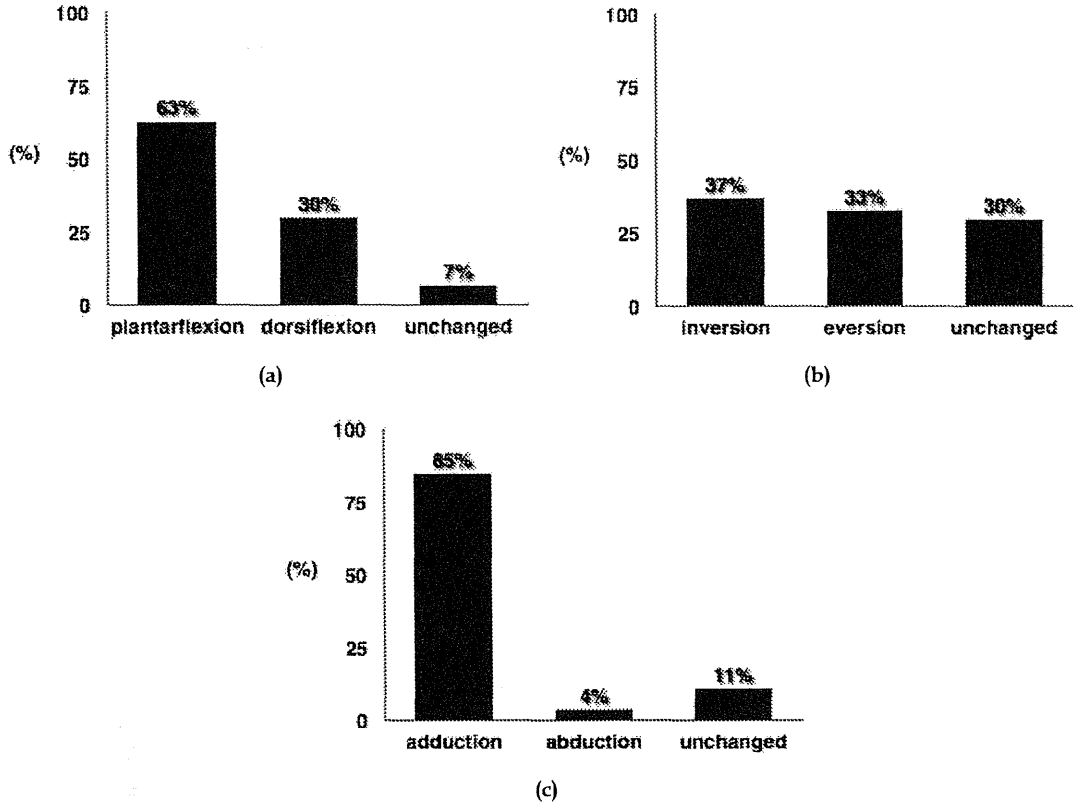

Fig. 5 Percentage of the feet grouped according to rotational directions in the sagittal **(a)**, coronal **(b)**, and transverse **(c)** planes.

rotations might be smaller than those under actual standing conditions. However, the rotational directions and patterns of the tibiotalar joint may not be influenced by smaller axial loadings. Second, the slice thickness of the MR images was 1.0 mm. As a result, analysis of minute motion was limited. Third, talus motion was investigated only in the neutral ankle position. Effects of ankle position were not investigated.

In the previous studies,[6,7,10] the results of three-axis rotational analysis of the tibiotalar joint under axial loading were combined as average values, even if there were variations in the rotational directions. Although all of the previous results[6,7,10] reported that the average sagittal rotational direction of the tibiotalar joint during axial loading was plantarflexion, our results revealed that the talus rotated into both plantarflexion and dorsiflexion relative to the tibia. Additionally, in the coronal plane, the talus also rotated into both inversion and eversion relative to the tibia, which might explain the reason for the inconsistent previous results[6,7,10] of the coronal inversion and eversion rotational directions at the tibiotalar joint. Kitaoka *et al.*[7] and Kido *et al.*[6] reported that the tibiotalar joint rotated into adduction under axial loading in the transverse plane, whereas only Michelson *et al.*[10] reported rotation into abduction. In this study, almost all of the tali consistently rotated into adduction relative to the tibia under axial loading.

There are probably several factors that determine the rotational directions of the tibiotalar joint under axial loading, including ligament

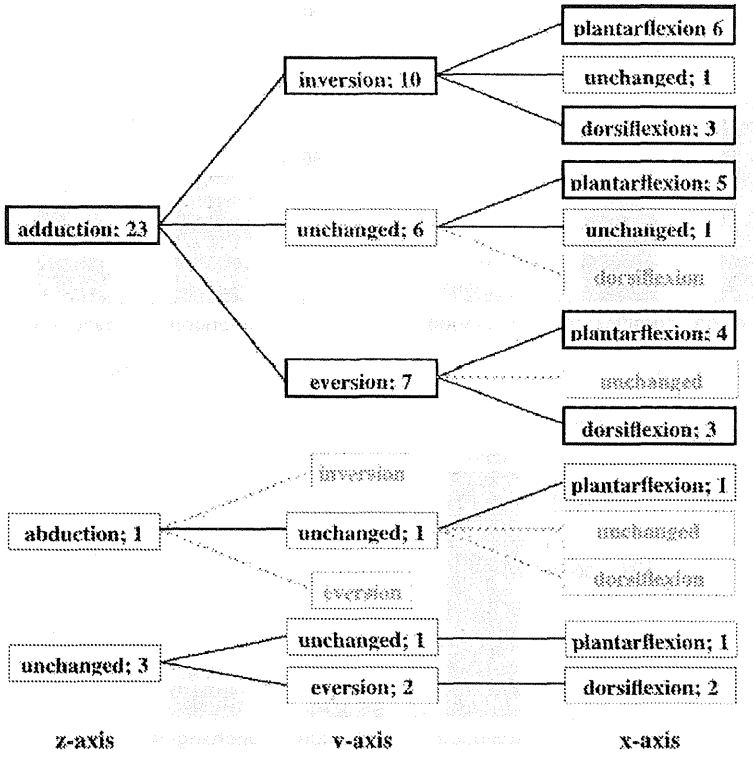

Fig. 6 Tree diagram representing the 3D rotational patterns and number of feet showing each pattern. The description in the boxed text describes the rotational direction and number of feet for each of the 3 axes. The 10 rotational patterns of the tibiotalar joint are shown.

Table 2 Number of Feet and Averages of the Three-Axis Rotations of the Tibiotalar Joint in the 10 Rotational Patterns.

Rotational Patterns	Number (%)	Rotations (Degrees)		
		x-axis	*y*-axis	*z*-axis
pf/iv/add	6 (22%)	3.3	1.2	1.3
pf/un/add	5 (18%)	1.2	—	1.2
pf/ev/add	4 (15%)	1.8	−0.7	1.1
df/iv/add	3 (11%)	−0.9	0.7	0.9
df/ev/add	3 (11%)	−0.7	−0.7	1.2
df/ev/un	2 (7%)	−1.7	−0.6	—
un/iv/add	1 (4%)	—	1.2	1.5
un/un/add	1 (4%)	—	—	0.9
pf/un/abd	1 (4%)	1.1	—	−2.6
pf/un/un	1 (4%)	0.6	—	—

Note: pf: plantarflexion, df: dorsiflexion, iv: inversion, ev: eversion, add: adduction, abd: abduction, un: unchanged.

laxity, structure of the tarsal bones, alignment of the lower extremity, and foot alignment, such as flat or high-arched foot. An important cause for the variations in three-axis rotational directions of the tibiotalar joint is thought to be the morphological variations in the talus and calcaneus. The sagittal direction of the talar head relative to the talar body has been reported to range widely from 70° to 107°.[8,9,12] During axial loading, the talus would be susceptible to shearing force at the talonavicular joint because the talus head is directed more proximally. Consequently, we inferred that tali with heads directed more proximally rotated into plantarflexion under axial loading, whereas tali with heads directed more distally rotated into dorsiflexion. In this study,

the rotational directions of the tibiotalar joint were mostly adduction in the transverse plane. This constant rotational direction of adduction at the tibiotalar joint was caused by the anatomical characteristics of the talar head that lies medial to the talar body.

In conclusion, we showed that the talus three-dimensionally rotated into 10 directions relative to the tibia under axial loading. Particularly, five main rotational patterns arising from the rotational variations in the sagittal and coronal planes were recognized, which accounted for 78% of the feet. The talus adducted in most of the subjects in the transverse plane. Our findings provide insight into the subject-specific kinematics of the tibiotalar joint. The study results may provide important baseline information for future studies that aim at elucidation of the pathogenesis of primary osteoarthritis or trauma of the ankle joint or that investigate the effects of pathological conditions or therapeutic procedures on ankle kinematics.

ACKNOWLEDGMENTS

The authors gratefully acknowledge the Department of Orthopedic Surgery at the Sapporo Medical University School of Medicine for the instrumental support in this work. The authors are also grateful to Hiroyuki Takashima, Hiroki Shishido, Rui Imamura, and Yoshihiro Akatsuka who belong to the Department of Radiology at Sapporo Medical University Hospital for collecting MR images. The technical assistance of Yoshihiko Fujita (NAC Image Technology Inc., Tokyo, Japan) and Tomoyuki Suzuki (Department of Orthopedic Surgery at the Sapporo Medical University School of Medicine) regarding data processing was greatly appreciated. Thank you to Dr. David J. Magee (Department of Physical Therapy, University of Alberta) for advising on the manuscript.

We declare that this submission is an original work and is not under consideration for publication by any other journal.

References

1. Barbaix E, Van Roy P, Clarys JP. Variations of anatomical elements contributing to subtalar joint stability: Intrinsic risk factors for post-traumatic lateral instability of the ankle? *Ergonomics* **43**(10): 1718–1725, 2000.
2. Bruckner J. Variations in the human subtalar joint. *J Orthop Sports Phys Ther* **8**(10): 489–494, 1987.
3. Bunning PS, Barnett CH. A comparison of adult and foetal talocalcaneal articulations. *J Anat* **99**: 71–76, 1965.
4. Forriol Campos F, Gomez Pellico L. Talar articular facets (facies articulares talares) in human calcanei. *Acta Anat (Basel)* **134**(2): 124–127, 1989.
5. Gupta SC, Gupta CD, Arora AK. Pattern of talar articular facets in Indian calcanei. *J Anat* **124**(3): 651–655, 1977.
6. Kido M, Ikoma K, Imai K, Maki M, Takatori R, Tokunaga D, Inoue N, Kubo T. Load response of the tarsal bones in patients with flatfoot deformity: In vivo 3D study. *Foot Ankle Int* **32**(11): 1017–1022, 2011.
7. Kitaoka HB, Lundberg A, Luo ZP, An KN. Kinematics of the normal arch of the foot and ankle under physiologic loading. *Foot Ankle Int* **16**(8): 492–499, 1995.
8. Mahato NK. Morphology of sustentaculum tali: Biomechanical importance and correlation with angular dimensions of the talus. *Foot (Edinb)* **21**(4): 179–183, 2011.
9. Mahato NK, Murthy SN. Articular and angular dimensions of the talus: Inter-relationship and biomechanical significance. *Foot (Edinb)* **22**(2): 85–89, 2012.
10. Michelson JD, Clarke HJ, Jinnah RH. The effect of loading on tibiotalar alignment in cadaver ankles. *Foot Ankle* **10**(5): 280–284, 1990.
11. Nakashima T, Hojo T. Variations in the talar articular facets of Japanese calcanei. *Fukuoka Igaku Zasshi* **77**(10): 544–548, 1986.
12. Peeters K, Schreuer J, Burg F, Behets C, Van Bouwel S, Dereymaeker G, Sloten JV, Jonkers I. Alterated talar and navicular bone morphology is associated with pes planus deformity: A CT-scan study. *J Orthop Res* **31**(2): 282–287, 2012.
13. Shahabpour M, Deville A, Van Roy P, Vaes P, De Mey J, De Maeseneer M. Magnetic resonance imaging of anatomical variants of the subtalar joint. *Surg Radiol Anat* **33**(7): 623–630, 2011.

14. Sharada R, Sneha K, Gupta C, Pai SR, Rairam GB. Non-metrical study of the pattern of talar articular facets in south Indian dry calcanei. *Surg Radiol Anat* **34**(6): 487–491, 2012.
15. Uygur M, Atamaz F, Celik S, Pinar Y. The types of talar articular facets and morphometric measurements of the human calcaneus bone on Turkish race. *Arch Orthop Trauma Surg* **129**(7): 909–914, 2009.
16. Yamaguchi S, Sasho T, Kato H, Kuroyanagi Y, Banks SA. Ankle and subtalar kinematics during dorsiflexion-plantarflexion activities. *Foot Ankle Int* **30**(4): 361–366, 2009.

執筆者一覧(執筆順)

蜂須賀研二	産業医科大学名誉教授
浅山　滉	長尾病院・参与
梅津祐一	小倉リハビリテーション病院・院長
橋元　隆	九州栄養福祉大学リハビリテーション学部教授
大丸　幸	九州栄養福祉大学リハビリテーション学部教授
深浦順一	国際医療福祉大学福岡保健医療学部教授・言語聴覚学
大峯三郎	九州栄養福祉大学リハビリテーション学部教授
浜村明徳	小倉リハビリテーション病院・名誉院長
佐伯　覚	産業医科大学若松病院・リハビリテーション科診療教授
大隈秀信	熊本託麻台リハビリテーション病院・リハビリテーション部部長
新小田幸一	広島大学大学院医歯薬保健学研究院教授
田中宏太佳	中部労災病院・リハビリテーション科部長
河津隆三	九州労災病院・リハビリテーション科部長
丹羽義明	九州労災病院・中央リハビリテーション部主任理学療法士
石橋敏郎	九州栄養福祉大学リハビリテーション学部准教授
大川裕行	西九州大学リハビリテーション学部教授
濱田哲郎	九州労災病院・中央リハビリテーション部主任理学療法士
江西一成	星城大学大学院健康支援学研究科教授
髙橋精一郎	九州栄養福祉大学リハビリテーション学部教授
明日　徹	産業医科大学病院・リハビリテーション部副技師長
坂本親宣	九州栄養福祉大学リハビリテーション学部教授
舌間秀雄	産業医科大学病院・リハビリテーション部技師長
木村美子	九州栄養福祉大学リハビリテーション学部教授
佐藤裕司	九州栄養福祉大学リハビリテーション学部准教授
佐野幹剛	九州栄養福祉大学リハビリテーション学部准教授
武本暁生	産業医科大学病院・リハビリテーション部療法科長
村上公照	九州労災病院・中央リハビリテーション部主任作業療法士
長尾哲男	九州栄養福祉大学リハビリテーション学部教授
成光瑞恵	前九州リハビリテーション大学校准教授
近藤　敏	県立広島大学保健福祉学部教授
吉田真理子	熊本保健科学大学保健科学部准教授
久野真矢	九州栄養福祉大学リハビリテーション学部教授
深町晃次	九州栄養福祉大学リハビリテーション学部講師
本村　暁	行橋記念病院・副院長

3 シャルコー・マリー・トゥース病，慢性炎症性脱髄性多発根神経炎

1 基礎的知識

a. シャルコー・マリー・トゥース病

シャルコー・マリー・トゥース病 Charcot-Marie-Tooth disease(CMT)は，遺伝性の末梢神経疾患であり，左右対称性に下肢遠位筋優位に筋萎縮や筋力低下が徐々に進行する．致死的な疾患ではなく寿命に影響しないが，歩行や巧緻動作などADLに障害を生じる．有効な治療法が確立されておらず，発症早期から適切なリハビリを行うことが大切である[5]．多くは青年期から中年期にかけて症状が進行するが，杖歩行を継続できる人から電動車椅子が必要となる人まで，障害の程度は一様でない．

脱髄型か軸索型か，遺伝形式(常染色体性優性，常染色体性劣性，X染色体性)，遺伝子座および原因遺伝子によって分類される[6]．近年，原因遺伝子が数多く明らかとなり，遺伝子異常に基づいた分類が行われるようになった．最も多いタイプは脱髄型のCMT1Aであり，ミエリン構成蛋白の*PMP22*(peripheral myelin protein 22)遺伝子の重複が原因である．CMTは遺伝的多様性があり，家系内でも症状や重症度が異なることもある．

b. 慢性炎症性脱髄性多発根神経炎

慢性炎症性脱髄性多発根神経炎 chronic inflammatory demyelinating polyradiculoneuropathy(CIDP)は，慢性進行性あるいは再発性に末梢神経に脱髄を生じる自己免疫性の末梢神経疾患である．四肢末梢の運動感覚障害を呈するが，臨床経過や症状は多岐にわたり，詳しい病態は明らかでない．症状はCMTと似ており，CMTの鑑別疾患として重要である．小児から高齢者まで幅広く発症し，やや男性に多い．わが国の成人での有病率は10万人あたり1.61人と報告されている[7]．治療として免疫グロブリン大量静注療法，血漿交換療法，副腎皮質ステロイド療法が有効である．

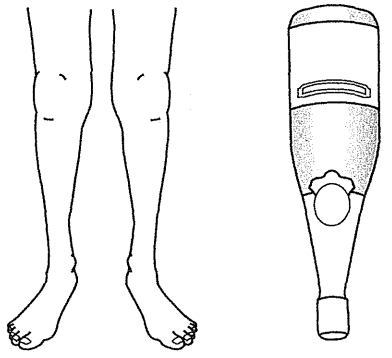

図 10-76　逆シャンペンボトル型の筋萎縮

図 10-77　凹足，槌趾

2 診断・評価

a. 診断

(1) CMT

病歴，家族歴，身体所見から本疾患を疑い，神経伝導検査と遺伝子検査によって確定診断される．四肢末梢の筋萎縮を生じ，四肢遠位筋ほど早期から障害されやすい．

下肢では，大腿 1/3 以下の遠位部ほど筋萎縮が目立つ逆シャンペンボトル型の筋萎縮（図 10-76）が特徴的であり，下垂足や凹足，槌趾を認める（図 10-77）．上肢では手内筋の筋萎縮を認め，鷲手や猿手を呈することがあり，そのため筋力は保たれていても巧緻動作障害を認める．神経伝導検査によって脱髄の障害か軸索の障害か診断し，遺伝子検査によって原因遺伝子を同定する．

(2) CIDP

臨床症状は多岐にわたるが，典型的な臨床症状は左右対称性の筋力低下，しびれであり，遠位筋だけでなく近位筋にも筋力低下を生じる．脳神経障害や呼吸筋障害を合併することもある．神経伝導検査で脱髄所見を確認する．

b. 評価

CMT，CIDP いずれも，ROM，四肢の筋力，筋萎縮の程度と範囲，手足の変形の有無，感覚障害，巧緻動作，歩行，ADL の評価を行う．下腿三頭筋の筋力低下があると静止立位を保持できない竹馬徴候を認める．歩行では下垂足による鶏歩が特徴的である．

3 治療プログラム

＃1 ROM 訓練，ストレッチ，＃2 筋力強化訓練，＃3 手指巧緻動作訓練，＃4 起立歩行訓練，＃5 装具の検討，＃6 自主訓練の指導

CMT に対する有効な治療がないため，診断を受けたあと，医療機関への受診やリハビリを行っていない症例が多い．しかし緩徐ではあるが症状が進行するため，リハビリと定期的なフォローを行う必要がある．リハビリは症状の進行に応じて行う．発症早期から手足の変形や拘縮の予防のため，ROM 訓練やストレッチが大切である．リハビリを十分量実施しても拘縮が改善しなければ，足部変形に対して腱延長術や骨切り術などの整形外科的治療も検討する．

筋力強化訓練は，低負荷・高頻度が基本であり，過負荷に注意する．CMT 患者では軽度から中等度の筋力強化訓練が有効で安全に行え，数週間の訓練を行うことで，下肢の筋力や歩行能力が改善したとの報告がある[8~13]．一般的に末梢神経障害では過用性筋力低下に注意が必要であるが，CMT でも過用性筋力低下を認める可能性がある[14]．

CIDP は，慢性の経過をたどり，再発，再燃した際には筋力低下や歩行の悪化がおこり，機能評価と症状に応じたリハビリが重要である．

4 リハビリテーションの実際

CMT，CIDP ともに発症早期から下腿三頭筋の持続伸張訓練を行うことが重要である．自重を

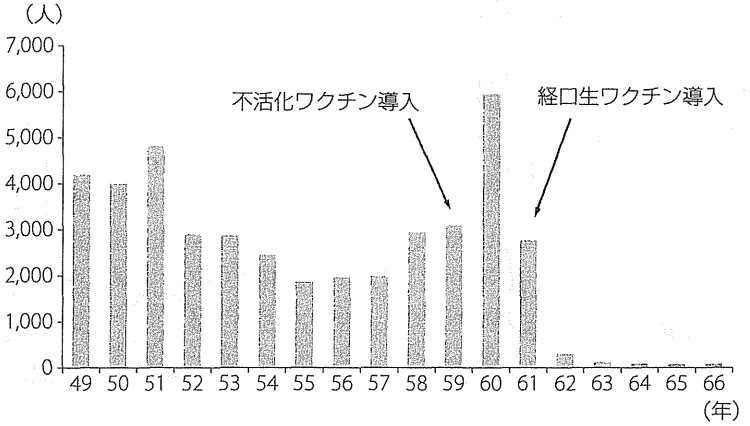

図 10-78　ポリオの発症

利用した起立台による下腿三頭筋の持続伸張訓練や，ストレッチが効果的である．また，踵の高い靴を履かないように指導することも大切である．足関節の背屈方向へのストレッチ，手指 MP 関節屈曲方向へのストレッチ，母指の対立位保持，股関節の伸展方向へのストレッチ，膝関節の伸展方向へのストレッチが重要である．温熱療法は，疼痛の緩和や局所の循環改善の目的で用いられ，ROM 訓練に先行して行えば，筋血流を良好な状態に保ち，組織の伸張性を増すことができる．

CMT では，一般的に仕事や通学，家事を行っており，活動性が高い症例に対しては積極的な筋力強化訓練は必要でなく，活動的な生活を継続するように指導する．活動的でない症例に対しては活動的な生活をすすめ，筋力強化訓練を指導する．筋力強化訓練は低負荷・高頻度で行う．過負荷に注意し，運動翌日に普段とは異なる筋力低下，筋肉痛，疲労感などを認める場合は，運動負荷を調整する．血液中のクレアチンキナーゼ(CK)を測定し，筋破壊の目安とする．CK 値が普段よりも急に高くなった場合，運動や生活強度が過剰であると判断し，運動量を減らす指導を行う．

また，手内筋の筋力低下に対しては，書字や箸の使用などの細かい動作の訓練や粘土細工などによる筋力強化訓練を指導する．

歩行障害に対しては，筋力に応じて適切な装具を選択することが大切であり，下垂足に対しては軟性装具やプラスチック製短下肢装具が用いられ，近位筋の筋力低下がある例では長下肢装具も用いられる．また，歩行が困難な症例には電動車椅子や電動補助車椅子の適応がある．手内筋の萎縮がある場合，手で把持する T 字杖などは使用しにくく，松葉杖やロフストランドクラッチ，プラットホーム型クラッチの使用がすすめられる．

4 ポリオ後症候群

1 基礎的知識

ポリオ後症候群 post-polio syndrome(PPS)とは，ポリオ罹患者が中高年になり，新たな筋力低下や歩行障害などの身体症状をきたす病態のことである．近年，ポリオ罹患者の高齢化に伴い PPS が大きな問題となってきた．

PPS の原疾患であるポリオは，ポリオウイルス 1 型，2 型，3 型による感染症である．ポリオウイルスに感染しても大部分は不顕性感染のみであり，微熱や咽頭痛などの非特異的症状を発現するのは感染者の 4〜8%，無菌性髄膜炎(非麻痺型)を生じるのは 1〜5%である．麻痺型はきわめて稀で，四肢に弛緩性麻痺を生じる脊髄障害型や，嚥下や呼吸障害を生じる延髄障害型は 0.1%にすぎない．わが国では 1960 年にポリオの大流行があったが，経口生ワクチンの導入により発症は急激に減少し，1980 年以降は野生株による発症は

Please cite this article in press as: Tamiya et al., A Mutation of *COX6A1* Causes a Recessive Axonal or Mixed Form of Charcot-Marie-Tooth Disease, The American Journal of Human Genetics (2014), http://dx.doi.org/10.1016/j.ajhg.2014.07.013

REPORT

A Mutation of *COX6A1* Causes a Recessive Axonal or Mixed Form of Charcot-Marie-Tooth Disease

Gen Tamiya,[1,*] Satoshi Makino,[1] Makiko Hayashi,[2] Akiko Abe,[2] Chikahiko Numakura,[2] Masao Ueki,[1] Atsushi Tanaka,[3] Chizuru Ito,[4] Kiyotaka Toshimori,[4] Nobuhiro Ogawa,[5] Tomoya Terashima,[5] Hiroshi Maegawa,[5] Daijiro Yanagisawa,[6] Ikuo Tooyama,[6] Masayoshi Tada,[7] Osamu Onodera,[7] and Kiyoshi Hayasaka[2,*]

Charcot-Marie-Tooth disease (CMT) is the most common inherited neuropathy characterized by clinical and genetic heterogeneity. Although more than 30 loci harboring CMT-causing mutations have been identified, many other genes still remain to be discovered for many affected individuals. For two consanguineous families with CMT (axonal and mixed phenotypes), a parametric linkage analysis using genome-wide SNP chip identified a 4.3 Mb region on 12q24 showing a maximum multipoint LOD score of 4.23. Subsequent whole-genome sequencing study in one of the probands, followed by mutation screening in the two families, revealed a disease-specific 5 bp deletion (c.247−10_247−6delCACTC) in a splicing element (pyrimidine tract) of intron 2 adjacent to the third exon of cytochrome *c* oxidase subunit VIa polypeptide 1 (*COX6A1*), which is a component of mitochondrial respiratory complex IV (cytochrome *c* oxidase [COX]), within the autozygous linkage region. Functional analysis showed that expression of *COX6A1* in peripheral white blood cells from the affected individuals and COX activity in their EB-virus-transformed lymphoblastoid cell lines were significantly reduced. In addition, *Cox6a1*-null mice showed significantly reduced COX activity and neurogenic muscular atrophy leading to a difficulty in walking. Those data indicated that *COX6A1* mutation causes the autosomal-recessive axonal or mixed CMT.

Charcot-Marie-Tooth disease (CMT) is the most common inherited neuromuscular disease characterized by clinical and genetic heterogeneity, which has been traditionally subdivided into two major subgroups, demyelinating and axonal forms. Initially, genes encoding major myelin proteins including peripheral myelin protein 22 (*PMP22* [MIM 601097])[1] and myelin protein zero (*MPZ* [MIM 159440])[2] were identified as genes involved in demyelinating CMT as well as mitofusin 2 (*MFN2* [MIM 608507])[3] in axonal CMT. So far, mutations causing CMT have been identified in more than 30 loci. To identify the genetic background of Japanese CMT, we analyzed the disease-causing mutation in about 350 affected individuals; however, we could not identify the causative mutations in about 50% of demyelinating CMT and 80% of axonal CMT.

We studied two families with affected members from consanguineous marriages at different sites in Japan (Figure 1A). The affected siblings of family 1 initially had slightly reduced median motor nerve conduction velocities (NCVs) and onion bulb formation in the sural nerve at young ages, but they had motor NCVs below 38 m/s when they were aged 30–39 years, indicating mixed CMT (Tables S1 and S2 available online). The affected member of family 2 had slightly reduced median motor NCVs at age 39, indicating axonal phenotype (Tables S3 and S4). Although the two families have no record of affinal connections each other, their affected members share similar disease phenotypes and a deduced mode of inheritance (i.e., recessive). Informed consent was obtained from all subjects, and all procedures were approved by the Research Ethics Committees of Yamagata University Faculty of Medicine and Niigata University School of Medicine. For these families, family 1 with two affected members from the marriage between second cousins and family 2 with one from that between first cousins once removed (Figure 1A), we carried out a parametric linkage study using genome-wide 6.5K SNP chip. A genome-wide SNP genotyping was performed for ten members from the two families with the HumanLinkage V Panel (Illumina). A multipoint linkage analysis was performed with Allegro v.2 and a human genetic map based on NCBI dbSNP Build 123 and identified a significant linkage in a 4.3 Mb region on 12q24 covered by nine SNPs showing multipoint LOD scores of 3.85–4.23 at $\theta = 0.00$ (Figures 1B, 1C, and S1; Table 1).

Subsequent whole-genome sequencing for the proband from family 1 was performed on a Genome Analyzer IIx system (Illumina), followed by annotation, filtering, and assessing potential effects of variants (Tables S5 and S6). It yielded enough data (a mean depth of 49.6×) to detect sequence variants by comparison with a reference sequence (Table S5). Of a total of 3,716,455 variants

[1]Advanced Molecular Epidemiology Research Institute, Faculty of Medicine, Yamagata University, Yamagata 990-9585, Japan; [2]Department of Pediatrics, Faculty of Medicine, Yamagata University, Yamagata 990-9585, Japan; [3]Research Institute of Medical Sciences, Faculty of Medicine, Yamagata University, Yamagata 990-9585, Japan; [4]Department of Reproductive Biology and Medicine, Graduate School of Medicine, Chiba University, Chiba 260-8670, Japan; [5]Department of Medicine, Shiga University of Medical Science, Otsu 520-2192, Japan; [6]Molecular Neuroscience Research Center, Shiga University of Medical Science, Otsu 520-2192, Japan; [7]Department of Molecular Neuroscience, Brain Research Institute, Niigata University, Niigata 951-8585, Japan
*Correspondence: gtamiya@genetix-h.com (G.T.), hayasaka@med.id.yamagata-u.ac.jp (K.H.)
http://dx.doi.org/10.1016/j.ajhg.2014.07.013.

Please cite this article in press as: Tamiya et al., A Mutation of *COX6A1* Causes a Recessive Axonal or Mixed Form of Charcot-Marie-Tooth Disease, The American Journal of Human Genetics (2014), http://dx.doi.org/10.1016/j.ajhg.2014.07.013

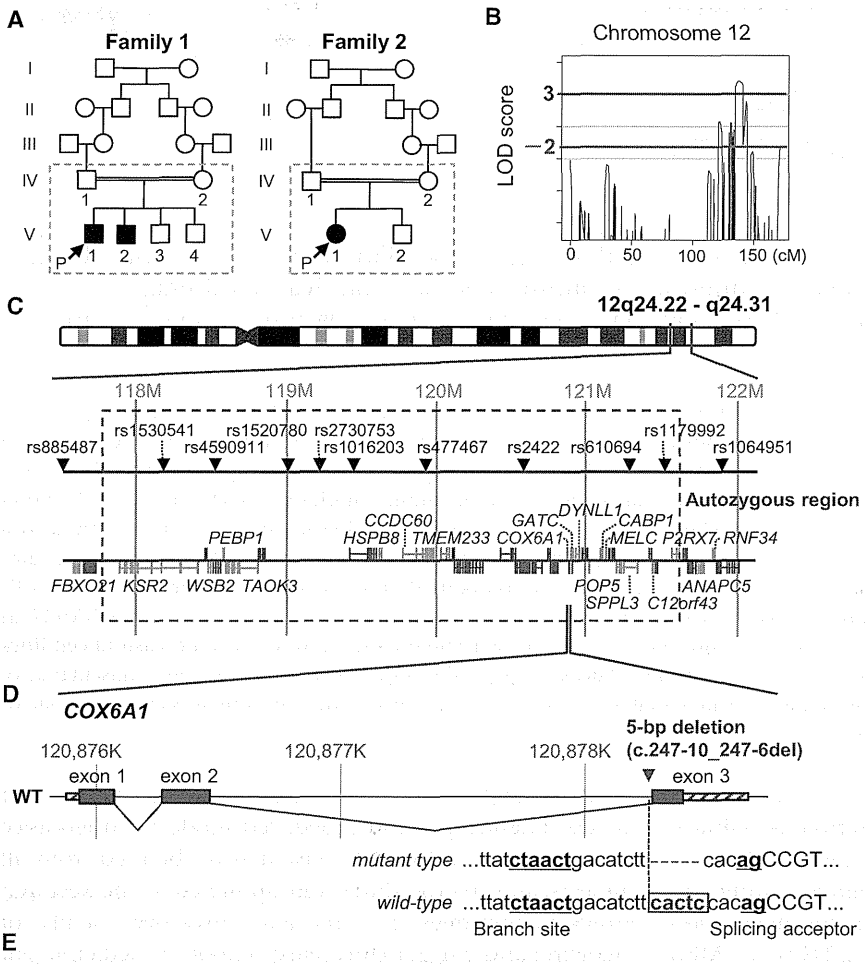

Figure 1. Genomic Analyses in the CMT Families

(A) Pedigrees of two consanguineous CMT families, from which a total of ten members in broken line boxes were sampled.

(B) Multipoint LOD scores on chromosome 12 using these ten members from two families with the HumanLinkage V SNP chip. We extracted genomic DNA from peripheral blood using the QIAamp DNA spin columns (QIAGEN) and quantified them using the Quant-iT PicoGreen dsDNA Assay Kit (Life Technologies). Genotyping was performed with the GoldenGate Genotyping Universal-32 kit on a BeadArray Reader System (Illumina) according to the manufacturer's assay guide. Genotype calls were made using the Genotyping module of the GenomeStudio v2009.1 software (Illumina). A multipoint linkage analysis was performed with Allegro v.2[4] and a human genetic map based on NCBI dbSNP Build 123 (see also Figure S1).

(C) Gene map in the significant linkage region on 12q24. These physical coordinates are taken from UCSC Genome Browser build hg19, RefSeq, and dbSNP 138 (UCSC Genome Browser database: 2014 update).

(D) A disease-specific 5 bp deletion (c.247–10_247–6delCACTC) in the pyrimidine tract near to the splicing acceptor near to the third exon of *COX6A1*.

(E) Validation and distribution of the 5 bp deletion among the CMT family members by Sanger-based PCR direct sequencing (see also Table S10).

(Table S7), after filtering out known or heterozygous variants, six were suspected to be deleterious by a majority rule approach using five prediction methods: PolyPhen-2, Grantham, PROVEAN, SIFT, and Mutation Taster (Table 2; see also Table S8 for a relaxed rule). Among them, only a 5 bp deletion (c.247–10_247–6delCACTC; RefSeq accession number NM_004373.3) was located just in a long run of homozygosity spanning 3.7 Mb, between rs10774925 and rs503720, in the significant linkage region on 12q24 (Figures 1C and 1D; Tables 1 and S9; see also Figure S2 and Table S10). In the two families, the 5 bp deletion was cosegregated perfectly with the disease state (Figures 1E and S3). Mutation screening by PCR assay detected the 5 bp deletion in none of 1,452 control chromosomes from diverse ethnic groups (Table S11).

As expected from the fact that this disease-specific 5 bp deletion disrupted an intronic splicing element (pyrimidine tract[11–13]) adjacent to the boundary of the second intron and the third exon of cytochrome *c* oxidase subunit VIa polypeptide 1 (*COX6A1* [MIM 602072]) whose expression is almost ubiquitous excepting skeletal muscles (see Su et al.[10] for human and Figure S4 for mouse), quantitative RT-PCR assay detected the significantly reduced (<1/5 of controls; $p < 0.001$) expression of the normally spliced form of *COX6A1* in peripheral white blood cells from two affected members of family 1 (Figure 2A, see also Table S12). Consistent with these findings, their cultured cell lines showed statistically significant reductions in the *COX6A1* expression ($p < 0.001$; Figure 2B, see also Table S12), cytochrome *c* oxidase (COX) activity (Figure 2C), and total ATP contents (Figure 2D) in these affected individuals relative to controls. Detailed descriptions are found in the legends of figures and tables for all experiments including expression analysis of *COX6A1* mRNA (see also Figure S5 and Table S12), determination of COX activity, and ATP amount. We performed two additional experiments: (1) the qRT-PCR using three

Please cite this article in press as: Tamiya et al., A Mutation of *COX6A1* Causes a Recessive Axonal or Mixed Form of Charcot-Marie-Tooth Disease, The American Journal of Human Genetics (2014), http://dx.doi.org/10.1016/j.ajhg.2014.07.013

Table 1. Multipoint LOD Scores on 12q24 and Estimated Haplotypes in the Significant Linkage Region

			Family 1												Family 2							
Markers	Positions[a]	LOD Score	IV-1 (Father)		IV-2 (Mother)		V-1 (Affected)		V-2 (Affected)		V-3 (Brother)		V-4 (Brother)		IV-1 (Father)		IV-2 (Mother)		V-1 (Affected)		V-2 (Brother)	
rs885487	117539934	−infinity	2	1	2	1	2	1	2	2	2	1	1	1	2*	2	2*	2	2*	2*	2*	2
rs1530541	118229731	4.0597	2*	2	2*	2	2*	2*	2*	2*	2*	2	2*	2	2*	1	2*	2	2*	2*	2*	1
rs4590911	118562757	4.2433	1*	2	1*	2	1*	1*	1*	1*	1*	2	1*	2	2*	2	2*	2	2*	2*	2*	2
rs1520780	119039725	4.2338	2*	1	2*	2	2*	2*	2*	2*	2*	1	2*	1	2*	2	2*	2	2*	2*	2*	2
rs2730753	119171974	4.2317	2*	1	2*	2	2*	2*	2*	2*	2*	1	2*	1	2*	2	2*	1	2*	2*	2*	2
rs1016203	119423542	4.2249	2*	2	2*	2	2*	2*	2*	2*	2*	2	2*	2	2*	2	2*	1	2*	2*	2*	2
rs477467	119927992	4.1386	2*	2	2*	1	2*	2*	2*	2*	2*	2	2*	2	2*	2	2*	2	2*	2*	2*	2
rs2422	120565188	4.0416	1*	2	1*	1	1*	1*	1*	1*	1*	2	1*	2	2*	2	2*	2	2*	2*	2*	2
5 bp del	120878247		+*	−	+*	−	+*	+*	+*	+*	+*	−	+*	−	+*	−	+*	−	+*	+*	+*	−
rs6106944	121304826	3.8859	2*	2	2*	2	2*	2*	2*	2*	2*	2	2*	2	1*	1	1*	2	1*	1*	1*	1
rs1179992	121495432	3.8466	1*	2	1*	2	1*	1*	1*	1*	2*	2	1*	2	2*	2	2*	1	2*	2*	2*	2
rs1064951	121878659	−1.7247	1	2	2	2	1	2	1	2	2	2	2	2	2*	2	2*	2	2*	2*	2*	2

Haplotypes were reconstructed using Allegro v.2 with "HAPLOTYPE" option from each family data including 5 bp deletion (c.247−10_247−6delCACTC). Asterisk indicates the putative disease-associated haplotypes in each family.
[a]Physical coordinate is taken from dbSNP 138 (UCSC Genome Browser, 2014 update).

primers specific to the mutant transcript showed its low level (Figure S6 and Table S12); and (2) the immunoblot showed no band at around 11.0 kDa for the mutant protein (Figure S7). These results suggest that the deletion leads to alternative splicing events triggering a potential nonsense-mediated RNA decay.

Finally, we examined commercially provided *Cox6a1*-null mice (Figure S8 and Table S13). All experimental procedures were performed according to the animal welfare regulations of Yamagata University Faculty of Medicine and Shiga University of Medical Science, and the study protocol was approved by the Animal Subjects Committee of Yamagata University Faculty of Medicine and Shiga University of Medical Science. The null mice showed lack of COX6A1 products (Figure 3A) and remarkable behavioral phenotypes including difficulty in walking (Figure 3B; Movie S1). Histological examinations revealed that the null mice had thinned sciatic nerves (Figure 3C) and neurogenic muscular changes including small angular fiber and small group atrophy (Figure 3D), although no remarkable neurodegeneration was found. In addition, consistent with the findings in the affected individuals, the null mice showed statistically significant reductions in COX activity and ATP contents in liver cells ($p < 0.001$; Figures 4A and 4B) and delayed motor NCV ($p < 0.01$; Figure 4C) relative to control animals.

Table 2. List of Homozygous and Potentially Deleterious Variants Nominated by at Least Three of Five Prediction Methods

		Alleles					Changes	
Chr	Start	Ref	Variant	Gene (MIM ID)	Types	Accession	Nucleotide	Protein
12	120878247	CACTC	−	*COX6A1*	splicing	NM_004373.3	c.247−10_247−6delCACTC	NA
2	114257705	C	−	*FOXD4L1* (MIM 611084)	frame-shift	NM_012184.4	c.876del	p.Gly293Alafs*151
14	24470691	−	A	*DHRS4L2* (MIM 615196)	frame-shift	NM_001193637.1	c.204_205insA	p.His69Thrfs*69
19	20807178	−	A	*ZNF626* (NA)	frame-shift	NM_001076675.2	c.1505dup	p.Ile503Hisfs*95
2	114257443	A	C	*FOXD4L1* (MIM 611084)	nonsynonymous	NM_012184.4	c.610A>C	p.Lys204Gln
8	126443464	G	T	*TRIB1* (MIM 609461)	nonsynonymous	NM_025195.3	c.320G>T	p.Arg107Leu

To assess potential variant effects for nonsynonymous variants, we used PolyPhen-2 v.2.2.2 (HumVar; score > 0.85),[5] Grantham Score from SeattleSeq Annotation v.137 (score > 151), PROVEAN v.1.1.3 (score < −2.5),[6] SIFT (score < 0.05),[7] and Mutation Taster (predicted as "disease causing")[8] and listed potentially deleterious variants voted by at least two prediction methods. Furthermore, we also referred gene expression in human whole brain on BioGPS (GeneAtlas U133A, gcrma data set)[9,10] (see also Table S8).

Please cite this article in press as: Tamiya et al., A Mutation of *COX6A1* Causes a Recessive Axonal or Mixed Form of Charcot-Marie-Tooth Disease, The American Journal of Human Genetics (2014), http://dx.doi.org/10.1016/j.ajhg.2014.07.013

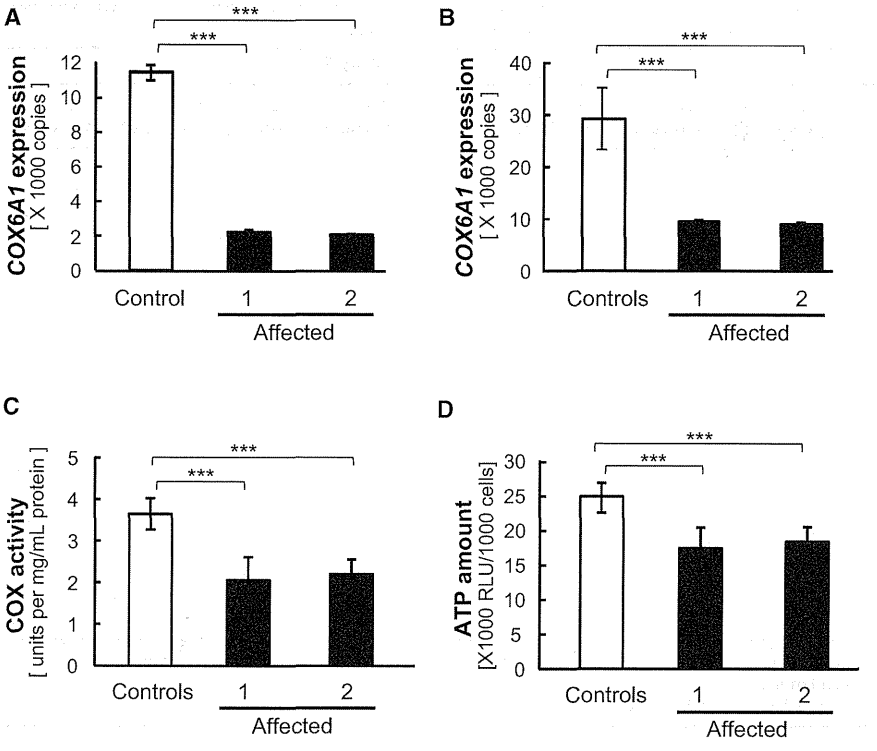

Figure 2. *COX6A1* Expression and COX Activity Levels

(A and B) *COX6A1* expression in fresh whole-blood from a control and the two affected individuals from family 1 (A) and in EBV-transformed B cell lines from four controls and the two affected individuals (B). Lymphoblastoid cells from two affected members in the family 1 were immortalized by infection with the Epstein-Barr virus (VR-1492; American Type Culture Collection). Immortalized cells from the four healthy Japanese individuals (HEV0031, HEV0032, HEV0038, and HEV0041) were provided by RIKEN BioResource Center. Total RNA was extracted using QIAamp RNA Blood Mini Kit or AllPrep DNA/RNA Kit (QIAGEN) according to the manufacturer's instructions with on-column DNase I treatment. After determining RNA concentrations using Quant-iT RiboGreen RNA Assay Kit (Life Technologies), 400 ng of total RNA per 40 μl reaction was used to synthesize cDNA using the High-Capacity cDNA Reverse Transcription Kit (Life Technologies) with random primers. Absolute quantification for *COX6A1* was performed using a custom TaqMan assay (Table S12). PCR products were ligated into pGEM-T easy vector (Promega) and isolated plasmid DNA was then linearized by EcoRI digestion. Before use, plasmid concentration was determined by Quant-iT PicoGreen dsDNA Assay Kit and serial dilutions were performed to generate standard curve. Real-time PCR was conducted using TaqMan Universal Master Mix II (Life Technologies) with a 7500 Fast real-time PCR system (Life Technologies). Each reaction was run in triplicate and contained 2 μl of cDNA template in a final reaction volume of 20 μl and data were analyzed with 7500 Software v.2.0.2.

(C and D) COX activity (C) and ATP amount (D) in mitochondrial fractions from the same four controls and two affected individuals' cell lines. For the determination of COX activity, we used a Cytochrome *c* Oxidase Assay kit (Sigma-Aldrich). Mitochondrial fractions were obtained from cells by homogenization in homogenization buffer (20 mM HEPES-KOH [pH 7.4], 220 mM mannitol, 70 mM sucrose, 1 mM EDTA, 1× protease inhibitor). The determination of COX activity was based on a colorimetric assay that quantifies the oxidation of ferrocytochrome *c* to ferricytochrome *c* via cytochrome *c* oxidase, a reaction that results in a decrease in absorbance at 550 nm. After measurement of absorbance, COX activity was calculated according to manufacturer's instructions. The amount of ATP was measured using a Lumino assay detecting cellular-ATP kit (CA100; Wako Pure Chemical Industries). The collected cells (1,000 cells per well) were used according to manufacturer's instructions. All experiments were triplicated per sample and tested using t test for the difference between controls mean and each affected individual mean. ***$p < 0.001$. The error bars represent the standard deviation.

Haplotype estimation around the linkage region reveals that the 5 bp deletion is harbored in background haplotypes that differ between family 1 and 2 (Tables 1 and S14; Figures S9 and S10), suggesting that this mutation occurred independently on each the haplotype origin. The two independent mutations in human CMT families and the null allele in mice consistently indicate that the 5 bp deletion can cause the disease phenotype through deficiency of *COX6A1* leading to the reduced COX activity in affected individuals' peripheral nerves as well. The *COX6A1* is expressed in the sciatic nerve as well as other tissues including lung, kidney, liver, and brain. Despite its expression in multiple tissues, the affected individuals carrying *COX6A1* mutation show no signs and symptoms other than that of the peripheral nervous system. It is interesting to note that the surfeit 1 (*SURF1* [MIM 185620]) encodes one of assembly factors of COX whose mutations cause demyelinating CMT accompanying with axonal loss[14] leading to multisystem involvement with nystagmus, hearing loss, kyphoscoliosis, and brain MRI abnormalities. In contrast, COX6A1 is small polypeptide required for the stability of holoenzyme. It is likely that the focal symptoms of our affected individuals are due to such narrow function, hypomorphic nature of the mutant allele, and/or the possibility for the residual amount of COX6A1 to warrant sufficient COX activity in other tissues as to maintain bioenergetic compensation. As another possibility, COX6A1 deficiency might be compensated by heart/muscle isoform, cytochrome *c* oxidase subunit VIa polypeptide 2 (COX6A2) in the other tissues or interfere with forming a stable COX assembly especially in the mitochondria of peripheral nervous system. Such mitochondrial respiratory chain deficiency might increase the vulnerability of nerve cells.[15–18] Finally, the tissue specificity might reflect the differential vulnerability to COX6A1 deficiency among them, as shown in many known examples such as TAF1 RNA polymerase II, TATA box binding protein (TBP)-associated factor, 250 kDa (TAF1),[19] huntintin (HTT),[20] and superoxide dismutase 1, soluble (SOD1).[21] However, a molecular mechanism

Please cite this article in press as: Tamiya et al., A Mutation of *COX6A1* Causes a Recessive Axonal or Mixed Form of Charcot-Marie-Tooth Disease, The American Journal of Human Genetics (2014), http://dx.doi.org/10.1016/j.ajhg.2014.07.013

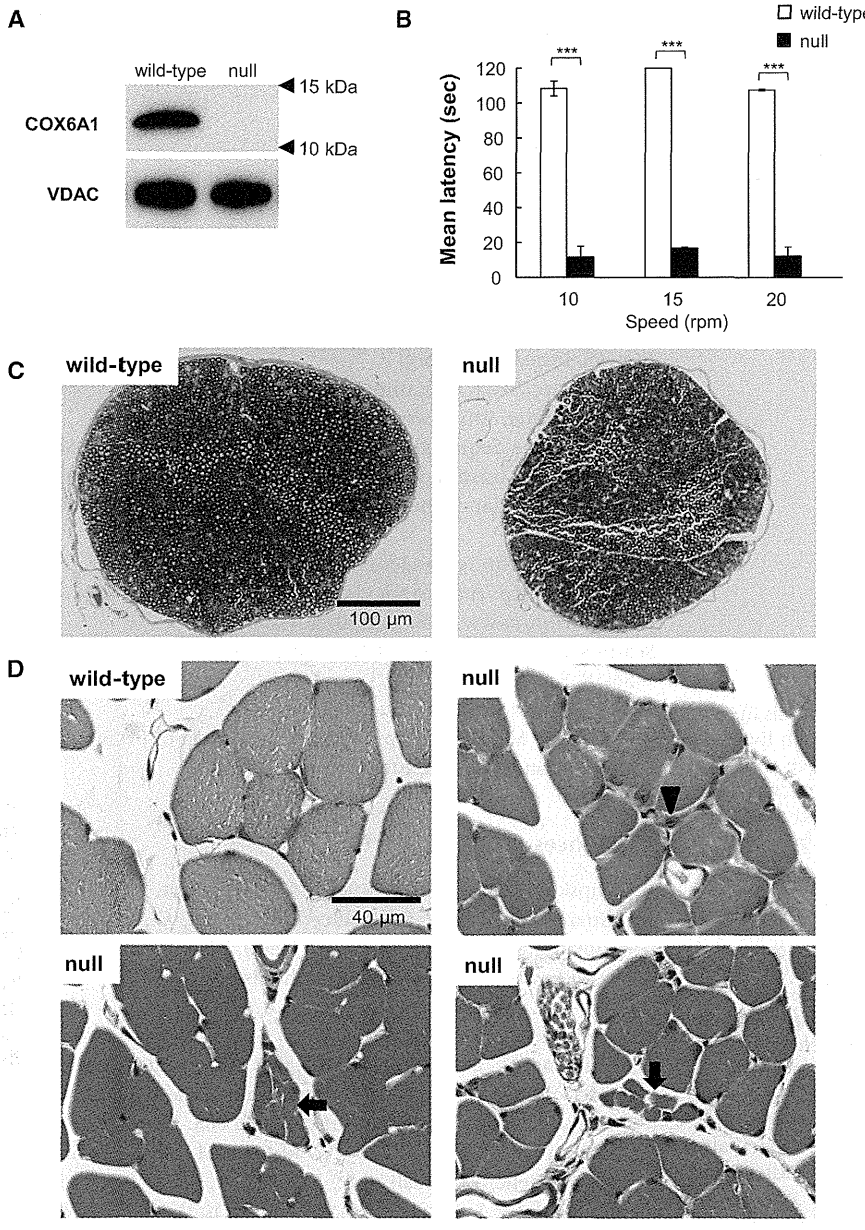

Figure 3. Characterization of *Cox6a1* Knockout Mice

(A) Immunoblot of COX6A1 and voltage-dependent anion channel (VDAC) as control in a wild-type and *Cox6a1* knockout null mice. Mice aged 7–8 weeks, three (one male and two female) knockout and three (two male and one female) wild-type were anesthetized and perfused with 10 mM PBS. Mitochondria fractions were obtained from liver tissue and applied to immunoblot. 20 μg of protein was loaded into a SDS-PAGE and transferred to the polyvinylidene difluoride membrane. The primary antibody for COX6A1 (mouse monoclonal, ab110265; abcam) is diluted 1:1,000 and secondary antibody for anti-COX6A1 (anti-mouse IgG, HRP-conjugated, 315-035-003; Jackson ImmunoResearch) is diluted 1:10,000. All blotting is carried out in 5% skim-milk/TBS solutions at room temperature for 1 hr.

(B) Motor coordination and balance was assessed as the latency to fall in the rota-rod. Mice aged 7–8 weeks, four (two male and two female) knockout and four (two male and two female) wild-type were used. Each mouse underwent the same 4 day procedure on a rota-rod (MK-660A; Muromachi Kikai). The first 3 days were used to train the mice (four sessions of 60 s each, walking at 20 rpm). The test sessions were run on the last day. The mice performed two series of three trials (10, 15, and 20 rpm) at each speed, with a 10 min rest period between trials. The latency to fall was recorded with a cut-off at 120 s. The difference between the wild-type and knockout null mice means were tested using t test. ***$p < 0.001$. The error bars represent the standard deviation.

(C and D) Histological examinations by toluidine blue staining sections of mice sciatic nerves at lower magnification (C) and hematoxylin-eosin staining sections of mice lower limb muscles (D). Arrow indicates a smaller number of fibers are involved in small group atrophy and arrowhead indicates small angular fibers despite the limited numbers. Mice aged 7–8 weeks, four (two male and two female) knockout and four (two male and two female) wild-type were anesthetized and perfused with 10 mM PBS, followed by a fixative of 4% paraformaldehyde (for leg muscle) or 2.5% glutaraldehyde (for sciatic nerve) in 0.1 M phosphate buffer. Sciatic nerve specimens were fixed in 2.5% glutaraldehyde in phosphate buffer for 2 hr at room temperature. After post-fixation with 1% OsO_4, the tissues were embedded in epoxy resin. Tissue blocks were sectioned at 1 mm thickness and stained with toluidine blue for light microscopic examination. For the histological analysis of leg muscle, mice tissues were postfixed in 4% paraformaldehyde for 48 hr at 4°C. The muscle tissues were dissected out and then incubated overnight in 10% sucrose in phosphate buffer. After snap freezing with CO_2 gas, tissue blocks were sectioned at 20 μm thickness in a cryostat and stained with hematoxylin and eosin.

between potential dysfunctions of the respiratory chain and the disease phenotype is still unclear. Our findings warrant further mechanistic analysis of structural analysis of COX holoenzyme, COX activity, and assembly in different tissues, including brain, heart, and, as a "positive control," skeletal muscle. To disentangle their high-order functional interplay, the results from our genetic study would warrant further mechanistic analyses of the mitochondrial involvements in the peripheral nervous system.

On the other hand, the multiple mutation events resulting in the same deletion in the pyrimidine tract imply that this site may be a mutational hotspot in human, so that there is a possibility that this deletion would be found across the world, especially from families with consanguineous loop, under the same scenario as Charcot-Marie-Tooth disease type 2F (CMT2F [MIM 606595])[22] or hereditary motor and sensory neuropathy, proximal type (HMSN-P [MIM 604484]).[23,24]

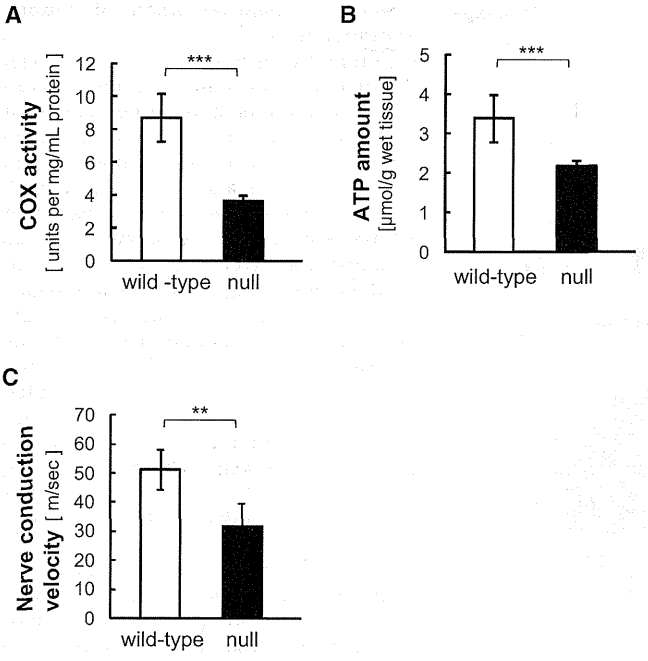

Figure 4. COX Activity and Electrophysiological Analysis in Mice
(A and B) COX activity in mitochondrial fractions from livers (A) and ATP amount in liver homogenates (B) from three wild-type and knockout null mice, respectively. Experiments for COX activity and ATP amount were triplicated per sample and all experiments were tested using t test for the difference between the wild-type and knockout mice means.
(C) Nerve conduction velocity of sciatic nerve from mice. Studies were demonstrated at 7–10 weeks of age, six (three male and three female) wild-type and seven (five male and two female) null mice with Sapphire (Medelec) under anesthesia of pentobarbital sodium (5 mg/kg i.p.). At the right dorsal femoral, sciatic nerve was exposed by opening up overlying skin and electrically stimulated using needle electrodes at the sciatic notch and at the knee joint level under 37°C ± 0.5°C. The compound muscle action potential (CMAP) evoked by the two parts of stimuli were recorded at gastrocnemius. Motor nerve conduction velocity (NCV) was calculated with dividing the distance between the sciatic notch and knee joint level by the delta latency between the two CMAP curves. Asterisks indicate the level of statistical significance (**$p < 0.01$; ***$p < 0.001$). The error bars represent the standard deviation.

Supplemental Data

Supplemental Data include 10 figures, 14 tables, and one movie and can be found with this article online at http://dx.doi.org/10.1016/j.ajhg.2014.07.013.

Acknowledgments

We would like to thank Kaoru Honaga, Michiyuki Kawakami, Akio Kimura, and Keiko Murayama for clinical information. This work was supported by Grant-in-Aid for Scientific Research from the Ministry of Education, Science, Sports and Culture of Japan to K.H. (grant number 25461537), A.A. (grant number 25860842), and G.T. (grant number 25129701) and Grant-in-Aid from the Global Center of Excellence program of the Japan Society for the Promotion of Science, "Formation of an International Network for Education and Research of Molecular Epidemiology."

Received: April 6, 2014
Accepted: July 29, 2014
Published: August 21, 2014

Web Resources

The URLs for data presented herein are as follows:

1000 Genomes, http://browser.1000genomes.org
BioGPS, http://biogps.org/
dbSNP, http://www.ncbi.nlm.nih.gov/projects/SNP/
MutationTaster, http://www.mutationtaster.org/
NHLBI Exome Sequencing Project (ESP) Exome Variant Server, http://evs.gs.washington.edu/EVS/
Online Mendelian Inheritance in Man (OMIM), http://www.omim.org/
PolyPhen-2, http://www.genetics.bwh.harvard.edu/pph2/
PROVEAN, http://provean.jcvi.org/index.php
RefSeq, http://www.ncbi.nlm.nih.gov/RefSeq
SeattleSeq Annotation 137, http://snp.gs.washington.edu/SeattleSeqAnnotation137/
SIFT, http://sift.bii.a-star.edu.sg/
SNP Genetic Mapping, http://integrin.ucd.ie/cgi-bin/rs2cm.cgi
UCSC Genome Browser, http://genome.ucsc.edu

References

1. Lupski, J.R., de Oca-Luna, R.M., Slaugenhaupt, S., Pentao, L., Guzzetta, V., Trask, B.J., Saucedo-Cardenas, O., Barker, D.F., Killian, J.M., Garcia, C.A., et al. (1991). DNA duplication associated with Charcot-Marie-Tooth disease type 1A. Cell *66*, 219–232.
2. Hayasaka, K., Himoro, M., Sato, W., Takada, G., Uyemura, K., Shimizu, N., Bird, T.D., Conneally, P.M., and Chance, P.F. (1993). Charcot-Marie-Tooth neuropathy type 1B is associated with mutations of the myelin P0 gene. Nat. Genet. *5*, 31–34.
3. Züchner, S., Mersiyanova, I.V., Muglia, M., Bissar-Tadmouri, N., Rochelle, J., Dadali, E.L., Zappia, M., Nelis, E., Patitucci, A., Senderek, J., et al. (2004). Mutations in the mitochondrial GTPase mitofusin 2 cause Charcot-Marie-Tooth neuropathy type 2A. Nat. Genet. *36*, 449–451.
4. Gudbjartsson, D.F., Jonasson, K., Frigge, M.L., and Kong, A. (2000). Allegro, a new computer program for multipoint linkage analysis. Nat. Genet. *25*, 12–13.
5. Adzhubei, I.A., Schmidt, S., Peshkin, L., Ramensky, V.E., Gerasimova, A., Bork, P., Kondrashov, A.S., and Sunyaev, S.R. (2010). A method and server for predicting damaging missense mutations. Nat. Methods *7*, 248–249.
6. Choi, Y., Sims, G.E., Murphy, S., Miller, J.R., and Chan, A.P. (2012). Predicting the functional effect of amino acid substitutions and indels. PLoS ONE *7*, e46688.
7. Kumar, P., Henikoff, S., and Ng, P.C. (2009). Predicting the effects of coding non-synonymous variants on protein function using the SIFT algorithm. Nat. Protoc. *4*, 1073–1081.
8. Schwarz, J.M., Rödelsperger, C., Schuelke, M., and Seelow, D. (2010). MutationTaster evaluates disease-causing potential of sequence alterations. Nat. Methods *7*, 575–576.
9. Wu, C., Orozco, C., Boyer, J., Leglise, M., Goodale, J., Batalov, S., Hodge, C.L., Haase, J., Janes, J., Huss, J.W., 3rd, and Su, A.I.

(2009). BioGPS: an extensible and customizable portal for querying and organizing gene annotation resources. Genome Biol. *10*, R130.

10. Su, A.I., Wiltshire, T., Batalov, S., Lapp, H., Ching, K.A., Block, D., Zhang, J., Soden, R., Hayakawa, M., Kreiman, G., et al. (2004). A gene atlas of the mouse and human protein-encoding transcriptomes. Proc. Natl. Acad. Sci. USA *101*, 6062–6067.
11. Lim, L.P., and Burge, C.B. (2001). A computational analysis of sequence features involved in recognition of short introns. Proc. Natl. Acad. Sci. USA *98*, 11193–11198.
12. Hirose, Y., Chiba, K., Karasugi, T., Nakajima, M., Kawaguchi, Y., Mikami, Y., Furuichi, T., Mio, F., Miyake, A., Miyamoto, T., et al. (2008). A functional polymorphism in THBS2 that affects alternative splicing and MMP binding is associated with lumbar-disc herniation. Am. J. Hum. Genet. *82*, 1122–1129.
13. Raben, N., Nichols, R.C., Martiniuk, F., and Plotz, P.H. (1996). A model of mRNA splicing in adult lysosomal storage disease (glycogenosis type II). Hum. Mol. Genet. *5*, 995–1000.
14. Echaniz-Laguna, A., Ghezzi, D., Chassagne, M., Mayençon, M., Padet, S., Melchionda, L., Rouvet, I., Lannes, B., Bozon, D., Latour, P., et al. (2013). SURF1 deficiency causes demyelinating Charcot-Marie-Tooth disease. Neurology *81*, 1523–1530.
15. Lin, M.T., and Beal, M.F. (2006). Mitochondrial dysfunction and oxidative stress in neurodegenerative diseases. Nature *443*, 787–795.
16. Suter, U., and Scherer, S.S. (2003). Disease mechanisms in inherited neuropathies. Nat. Rev. Neurosci. *4*, 714–726.
17. Pitceathly, R.D., Murphy, S.M., Cottenie, E., Chalasani, A., Sweeney, M.G., Woodward, C., Mudanohwo, E.E., Hargreaves, I., Heales, S., Land, J., et al. (2012). Genetic dysfunction of MT-ATP6 causes axonal Charcot-Marie-Tooth disease. Neurology *79*, 1145–1154.
18. Rinaldi, C., Grunseich, C., Sevrioukova, I.F., Schindler, A., Horkayne-Szakaly, I., Lamperti, C., Landouré, G., Kennerson, M.L., Burnett, B.G., Bönnemann, C., et al. (2012). Cowchock syndrome is associated with a mutation in apoptosis-inducing factor. Am. J. Hum. Genet. *91*, 1095–1102.
19. Makino, S., Kaji, R., Ando, S., Tomizawa, M., Yasuno, K., Goto, S., Matsumoto, S., Tabuena, M.D., Maranon, E., Dantes, M., et al. (2007). Reduced neuron-specific expression of the TAF1 gene is associated with X-linked dystonia-parkinsonism. Am. J. Hum. Genet. *80*, 393–406.
20. Sawa, A., Wiegand, G.W., Cooper, J., Margolis, R.L., Sharp, A.H., Lawler, J.F., Jr., Greenamyre, J.T., Snyder, S.H., and Ross, C.A. (1999). Increased apoptosis of Huntington disease lymphoblasts associated with repeat length-dependent mitochondrial depolarization. Nat. Med. *5*, 1194–1198.
21. Pasinelli, P., and Brown, R.H. (2006). Molecular biology of amyotrophic lateral sclerosis: insights from genetics. Nat. Rev. Neurosci. *7*, 710–723.
22. Evgrafov, O.V., Mersiyanova, I., Irobi, J., Van Den Bosch, L., Dierick, I., Leung, C.L., Schagina, O., Verpoorten, N., Van Impe, K., Fedotov, V., et al. (2004). Mutant small heat-shock protein 27 causes axonal Charcot-Marie-Tooth disease and distal hereditary motor neuropathy. Nat. Genet. *36*, 602–606.
23. Maeda, K., Kaji, R., Yasuno, K., Jambaldorj, J., Nodera, H., Takashima, H., Nakagawa, M., Makino, S., and Tamiya, G. (2007). Refinement of a locus for autosomal dominant hereditary motor and sensory neuropathy with proximal dominancy (HMSN-P) and genetic heterogeneity. J. Hum. Genet. *52*, 907–914.
24. Lee, S.S., Lee, H.J., Park, J.M., Hong, Y.B., Park, K.D., Yoo, J.H., Koo, H., Jung, S.C., Park, H.S., Lee, J.H., et al. (2013). Proximal dominant hereditary motor and sensory neuropathy with proximal dominance association with mutation in the TRK-fused gene. JAMA Neurol. *70*, 607–615.

INTERNAL MEDICINE

□ CASE REPORT □

Partial Deficiency of Emerin Caused by a Splice Site Mutation in *EMD*

Junhui Yuan[1], Masahiro Ando[1], Itsuro Higuchi[1], Yusuke Sakiyama[1], Eiji Matsuura[1], Kumiko Michizono[1], Osamu Watanabe[1], Shinjiro Nagano[2], Yukie Inamori[1], Akihiro Hashiguchi[1], Yujiro Higuchi[1], Akiko Yoshimura[1] and Hiroshi Takashima[1]

Abstract

Emery-Dreifuss muscular dystrophy (EDMD) is caused by mutations in the *EMD* gene on the X chromosome, which codes for emerin, an inner nuclear membrane protein. Monoclonal antibodies against the N-terminus of emerin protein are used to screen for emerin deficiency in clinical practice. However, these tests may not accurately reflect the disease in some cases. We herein describe the identification of a splice site mutation in the *EMD* gene in a Japanese patient who suffered from complete atrioventricular conduction block, mild muscle weakness and joint contracture, and a persistently elevated serum creatine kinase level. We used multiple antibodies to confirm the presence of a novel truncating mutation in emerin without the transmembrane region and C-terminus in the skeletal muscle.

Key words: Emery-Dreifuss muscular dystrophy (EDMD), splice site mutation, emerin, immunohistochemical stain

(Intern Med 53: 1563-1568, 2014)
(DOI: 10.2169/internalmedicine.53.8922)

Introduction

Emery-Dreifuss muscular dystrophy (EDMD) is characterized by early contractures of the elbow, neck, and Achilles tendons; slowly progressive skeletal muscle wasting in the upper arms and lower legs (humeroperoneal); and cardiomyopathy associated with conduction defects (1). The most serious aspect of EDMD is cardiac involvement, which usually becomes evident as muscle weakness progresses, but it may occur before there is any significant skeletal muscle involvement. EDMD is caused by mutations in different genes; including those in the *EMD* gene, encoding emerin, and causing X-linked EDMD (2); mutations in the *LMNA* gene, which encodes lamins A and C, and causes autosomal dominant EDMD (3) and a very rare autosomal recessive EDMD (4).

Monoclonal antibodies against the N-terminus of emerin, including Novocastra™ Lyophilized Mouse Monoclonal Antibody Emerin (NCL-emerin), have been used to screen emerin deficiency in clinical practice. In general, previous studies only used one kind of antibody in western blot or immunocytochemistry tests to evaluate emerin expression. Most of the mutations (86%) affecting males result in a complete absence of emerin (5); however, the corresponding genotypes were different, indicating that pathological assessments using a single antibody could not accurately reflect patients' diverse genetic information.

We herein describe the case of a patient with typical complete atrioventricular conduction block along with mild muscle weakness and joint contracture. We identified a previously reported splice acceptor site mutation in *EMD*, but the original symptoms and clinical severity of our case are different from those of the previous patient with this mutation (6). Furthermore, immunohistochemistry using three antibodies against different emerin domains revealed a distinct partial deficiency of emerin in the nuclei of the skeletal muscle fibers.

[1]Department of Neurology and Geriatrics, Kagoshima University Graduate School of Medical and Dental Sciences, Japan and [2]Department of Cardiology, Imamura Bun-in Hospital, Japan
Received for publication September 5, 2012; Accepted for publication January 30, 2014
Correspondence to Dr. Hiroshi Takashima, thiroshi@m3.kufm.kagoshima-u.ac.jp